NASA TECHNICAL NOTE

c. 1

NASA TN D-3882

BOUNDARY-LAYER MEASUREMENTS IN ACCELERATED FLOWS NEAR MACH 1

by Howard L. Wesoky

Lewis Research Center

Cleveland, Ohio

NATIONAL AERONAUTICS AND SPACE ADMINISTRATION • WASHINGTON, D. C. • MARCH 1967

BOUNDARY-LAYER MEASUREMENTS IN ACCELERATED

FLOWS NEAR MACH 1

By Howard L. Wesoky

Lewis Research Center
Cleveland, Ohio

BOUNDARY-LAYER MEASUREMENTS IN ACCELERATED FLOWS NEAR MACH 1

by Howard L. Wesoky

Lewis Research Center

SUMMARY

Experimental velocity and temperature profiles for the adiabatic boundary layers on cylindrical bodies in parallel accelerated flows are presented. Measurements were made near Mach 1 with the accelerations imposed by two axisymmetric nozzles having large differences in pressure gradient. The effects of boundary-layer tripping and development length were examined. Velocity profiles compared on a power profile basis yielded values for the exponent in the range 1/2.1 to 1/11.0. Comparison of the velocity profiles to two forms for the "law of the wall" and the Deissler prediction method (NASA Technical Report R-17) yielded good results when used with the Coles friction law. A significant effect of pressure history on friction coefficient was observed, which could be related to a nonadiabatic flow field through Reynolds analogy. The measured temperature profiles did not compare as well as the velocity profiles with the theories of Rotta or Deissler. The common assumption of constant boundary-layer total temperature for adiabatic flow was confirmed.

INTRODUCTION

Reliable estimates of the heat-transfer rates must be available in order to optimize the design of rocket nozzles. Common methods of prediction rely heavily on an approximation to the boundary-layer velocity profile (ref. 1), which is generally based on experimental data measured under incompressible and zero pressure gradient flow conditions. As a result of the inaccuracies in predicting heat transfer in the throat region of rocket nozzles, the velocity profile approximations have come in question, and a series of measurements to evaluate the effects of nozzle flow on boundary-layer velocity profiles is justified.

Other investigations of a similar nature have indicated that such relations as the 1/7-power velocity profile or the "law of the wall" universal profile yield adequate

approximations of the nozzle boundary layer when the streamwise pressure gradients are mild. Sibulkin (ref. 2) has measured boundary-layer velocity profiles in a supersonic wind tunnel near the throat and has reported that the data agreed well with a 1/7-power velocity profile as well as the von Karman universal profile used in conjunction with the Blasius friction law for incompressible turbulent flow. In reference 3, data are presented for velocity profile measurements on cylindrical bodies in parallel flow in the test section of a supersonic wind tunnel. Pressure gradient effects were examined with measurements in regions of varying test body cross-section area. Good agreement was indicated between the data and the Rotta "law of the wall" profile (ref. 3) used with an incompressible friction law. This velocity relation considers compressibility, but not pressure gradient effects.

The data of reference 4, which reports a nozzle heat-transfer experiment, indicate that the standard prediction techniques used with such good results in references 2 and 3 may not be adequate when applied to rocket type nozzles. Velocity profile measurements were made in a cylindrical inlet and slightly downstream of the entrance to the 30°-half-angle convergent nozzle section. The inlet boundary-layer velocity profile was of the 1/7-power type, but the nozzle measurement, made at a free-stream Mach number of about 0.08, produced a very flat profile which could be approximated by a 1/20- or 1/30-power velocity profile. Similar results were obtained when the nozzle was cooled and when the flow was adiabatic. The cause of the drastic change in velocity profile was not clear, but was generally believed to be connected with the acceleration effects of the streamwise pressure gradient and the wall curvature.

The present experiments eliminate the effect of wall curvature, which existed in references 2 to 4, and concentrate on the acceleration effect of the pressure gradient. Velocity profile measurements were made on two cylindrical bodies in parallel flow in two axisymmetric nozzles. The measurements were made near the throats of the nozzles, which had large differences in radii of curvature to produce correspondingly large differences in pressure gradient. The cylindrical bodies varied in length so an assessment could be made of the effect of boundary-layer development length. Boundary-layer tripping was also examined. Instrumentation used to measure velocity consisted of small pitot tubes and bare wire thermocouples.

The scope of the present work is to present results of the measurements and to compare these measurements with standard prediction techniques, so as to assess the applicability of these techniques.

SYMBOLS

a   sonic velocity, ft/sec

C_f friction coefficient (see eq. (13))

2

$\overline{C}_f$ low-speed friction coefficient

C_1, C_2 constants for "law of the wall" (see eq. (15))

D_t equivalent throat diameter, in.

M Mach number, u/a

M_τ Rotta Mach number parameter (see eq. (15))

n denominator of exponent in velocity power law (see eq. (10))

P pressure, psi

R recovery ratio, T_R/T_T

$\overline{R}$ gas constant, (ft)(lb force)/(lb mass)(^{O}R)

R_e unit Reynolds number (1-ft length), $\rho_e u_e/\mu_e$

$\overline{R}_e$ low-speed Reynolds number

r recovery factor, $(T_R - T)/(T_T - T)$

T temperature, ^{O}R

T^+ dimensionless static temperature (see eq. (18))

u velocity, ft/sec

u^+ dimensionless velocity (see eq. (12))

x axial distance, in.

y radial distance from cylinder surface, in.

y^+ dimensionless distance (see eq. (11))

γ specific heat ratio

δ boundary-layer velocity thickness, in.

δ^* displacement thickness (see eq. (7)), in.

θ momentum thickness (see eq. (9)), in.

μ dynamic viscosity, lb mass/(sec)(ft)

ρ density, lb mass/cu ft

σ_t turbulent Prandtl number

τ shear stress, lb/sq ft

Subscripts:

e boundary-layer edge

o   free-stream total condition

R   probe recovery condition

T   local total condition

T_2 total condition downstream of normal shock

w   wall condition

δ velocity thickness

δ^* displacement thickness

θ momentum thickness

$\bar{\theta}$ low-speed momentum thickness

APPARATUS

Flow System

A diagram of the flow system is shown in figure 1. The air source was a 55-psi combustion air supply expanded to near atmospheric pressure. This supply was used because of the low moisture content of the air, about 1.5 grains per pound of dry air, which allowed flow free from condensation (ref. 5). The air was mixed in a plenum by flowing from a large perforated pipe against the side walls of the plenum and then through a fiber-glass blanket filter into the bell mouth entrance of the nozzle. The filter was necessary to remove rust particles, which entered with the dry air. The filter removed 100 percent of the particles above 50 microns in size and 90 percent of the particles between 10 and 50 microns in size, but dust was still found on the instrumentation. An analysis revealed the dust to be of submicron size and thus nearly impossible to remove from the flow. The only effect was a sand blasting of the upstream side of all instrumentation placed in the air flow. No rust particles were found in the pitot-tube mouths. After passing through the test section, the air was exhausted into a 2-psi exhaust system. This back pressure caused the starting shock to be positioned far downstream of the test section.

The plenum pressure was measured with a manometer referenced to the atmosphere. The plenum temperature was measured with a bare wire copper-constantan thermocouple placed at the side of the bell mouth inlet. A hot-wire anemometer measurement was made at the center of the entrance plane of the bell mouth inlet and yielded a turbulence intensity of approximately 4 percent.
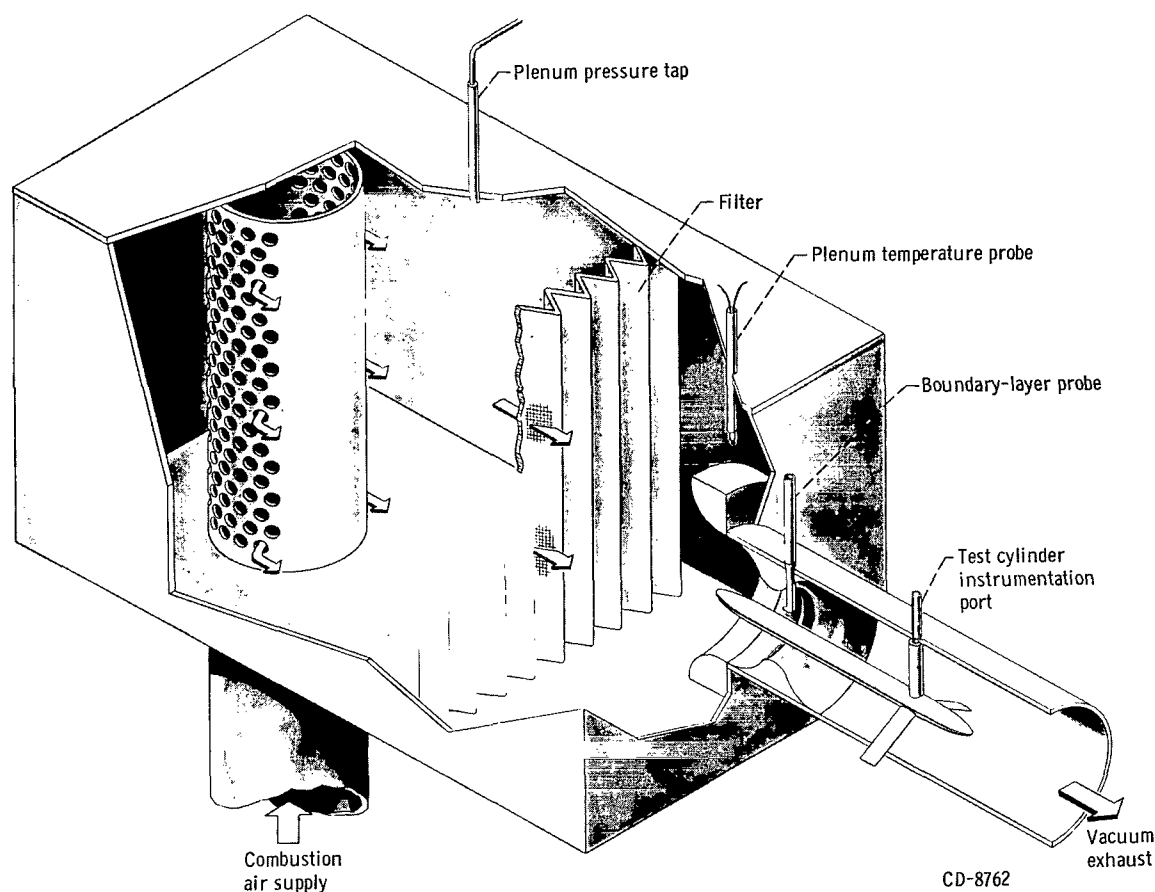
Figure 1. - Flow system. Free-stream total pressure, $\simeq 14.3$ psi; free-stream total temperature, $\simeq 540°$ R.

Test Nozzles

The two axisymmetric test nozzles were made of a hard wood and were given a very smooth lacquered finish. They were each cemented and bolted inside an 8-inch-inside-diameter steel pipe for mounting in the flow system. The geometry of the nozzles consisted of circular arc throats faired into fifth-order polynomial curves, which assured continuity in the shapes of the nozzles through the second derivative. The dimensions of the nozzles are given in table I (p. 6). Instrumentation access through the nozzle walls was obtained with long slits running downstream of the test section.

In each case, the position of the test station was chosen as close as possible to the nozzle throat without changing the position of the geometric throat due to instrument blockage. This position resulted in a test section free-stream Mach number of 1.17 for the nozzle having the larger radius of curvature and 1.08 for the other nozzle. These

5

TABLE I. - NOZZLE COORDINATES
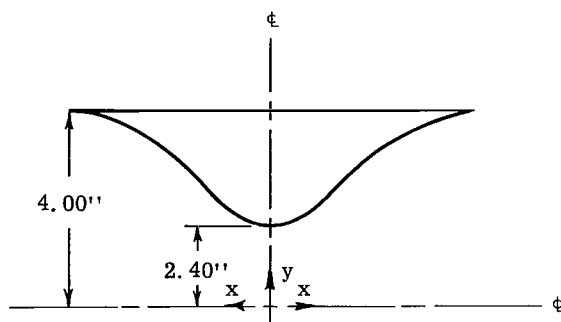
| Low-gradient nozzle[a]		High-gradient nozzle[b]	
Axial distance, x, in.	Radial distance, y, in.	Axial distance, x, in.	Radial distance, y, in.
0	2.40	0	2.40
3.93	2.61	1.91	3.39
4.00	2.62	2.00	3.50
4.50	2.70	2.10	3.62
5.00	2.86	2.25	3.74
5.50	3.11	2.40	3.84
6.00	3.40	2.60	3.90
6.50	3.68	2.75	3.96
7.00	3.88	2.90	3.98
8.00	4.00	3.00	4.00

[a]Throat radius of curvature, 36.77 in.

[b]Throat radius of curvature, 2.35 in.

nozzles will be referred to as the "low-gradient nozzle" and the "high-gradient nozzle," respectively, so as to emphasize the relative pressure gradients.

Test Cylinders

A diagram of the test cylinders is shown in figure 2. They consisted of 1-inch-diameter brass tubes having a 0.125-inch wall thickness. A threaded steel rod ran the length of the short cylinder, and aluminum ogive sections were screwed on both ends. The longer test cylinder was constructed by removing the upstream ogive section of the short cylinder and replacing it with a brass extension to which the ogive section and a strut support were connected. While the short cylinder was a cantilever structure, the long cylinder was supported at both ends, the upstream end being supported by two

(a) Short cylinder.

CD-8763
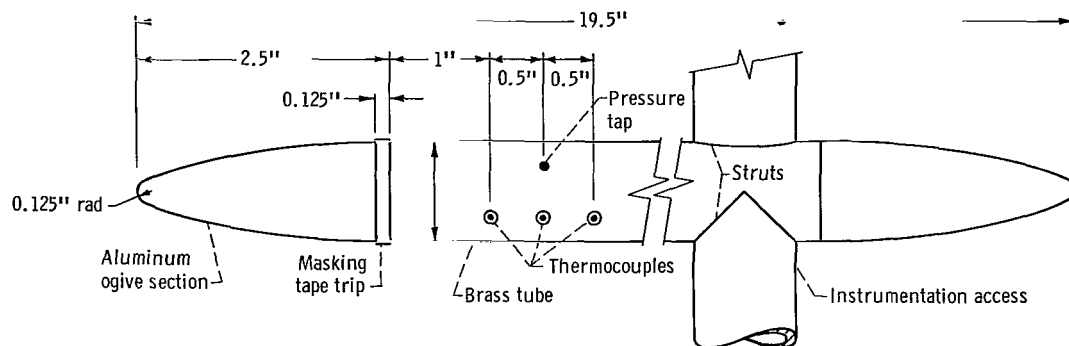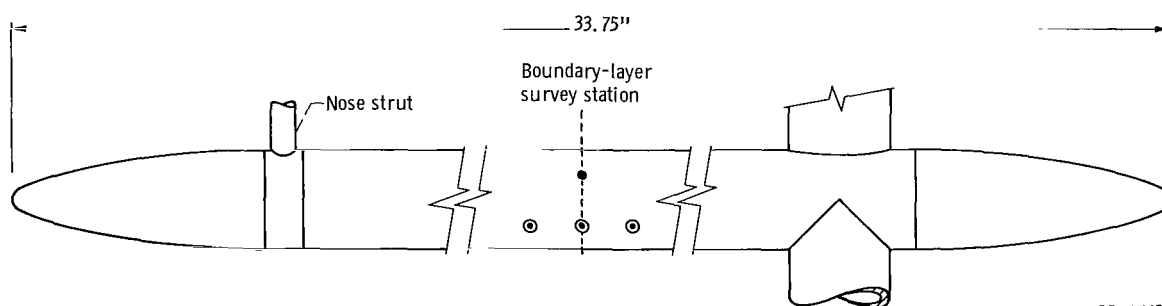
(b) Long cylinder.
Figure 2. - Test cylinders.

circular struts 90° apart and approximately diametrically opposed to the measuring station. The struts were anchored to the bell mouth inlet.

The short cylinder was instrumented with eight copper-constantan thermocouples on the surface. Four thermocouples were placed 90° apart at the axial test station. Two thermocouples were 0.5 inch upstream of the test section, 180° apart, and two thermocouples were 0.5 inch downstream of the test section, also 180° apart. Two 0.020-inch-diameter static pressure taps, 180° apart, were placed at the test section. A self-balancing potentiometer was used to record the thermocouple temperatures, and a mercury manometer, referenced to the atmosphere, was used to record the test section static pressure. The extension piece, used to form the longer cylindrical body, had no instrumentation.

To check whether or not the flow was shock free and to measure the pressure gradient at the test section required the construction of a third test cylinder, identical in geometry to the short cylinder previously described. The third cylinder was used to

measure the static pressure distribution along the nozzle axes and had twenty-one 0.020-inch-diameter pressure taps arranged in a spiral, 0.250 inch apart, along the cylinder axis beginning at the stagnation point. The 11 upstream taps were connected to acetylene tetrabromide manometers referenced to the atmosphere, and the remaining taps were connected to mercury manometers also referenced to the atmosphere.

The boundary-layer trips were formed with two layers of 0.125-inch-wide masking tape, which provided an obstacle approximately 0.015 inch high in the flow. The trip on the short cylinder was placed at the upstream side of the interface between the ogive section and the constant area section (fig. 2, p. 7), and the long cylinder's trip was at the upstream side of the interface between the short cylinder and the extension piece. With both the high- and low-gradient nozzles, tripped and untripped boundary-layer measurements were made on the short and the long test cylinders.
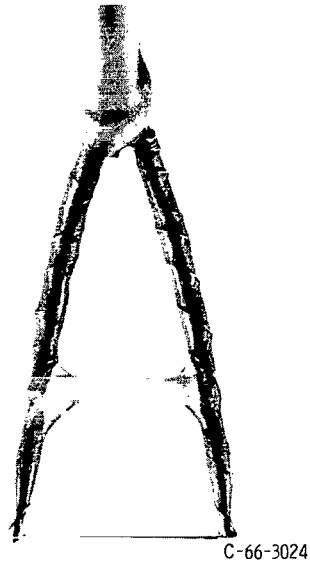
Pitot Tubes

A diagram of the general geometry of the pitot tubes, along with a photograph of the tube mouth, is shown in figure 3. In an attempt to discern any effect of pitot-tube geometry on boundary-layer measurements, three sizes of tube mouths were used. The tube mouths were formed from 28-mil stainless-steel tubes, and when finished the rectangular openings were 30 mils wide with heights of 1.5, 2.0, and 4.0 mils. The effect of pitot-tube height will be discussed in the RESULTS AND DISCUSSION section.

A calibration of the pressure recovery characteristics of the pitot tubes was conducted at constant static pressure in a free jet over the range $M = 0$ to 1. Normal shock relations (ref. 6) were used to extend the calibration beyond $M = 1$. The results of the calibration revealed that the isentropic relation (ref. 6) between the static to the total pressure ratio and the Mach number could be used in the data reduction without introducing any significant errors.
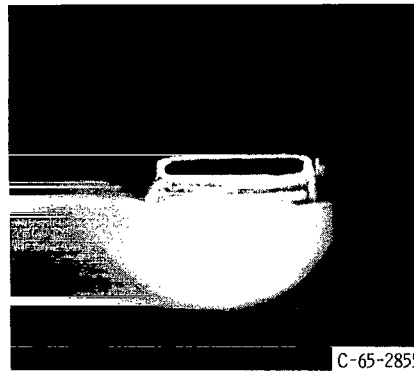
Manometer tubes referenced to the atmosphere were used for the pitot-tube measurements. For the portion of the boundary layer closest to the cylinder, where the pressure differences were large, a mercury manometer was used. For the outer portion of the boundary layer, where pressure differences were small, a manometer fluid having a lower specific gravity was used.

Thermocouple Probe
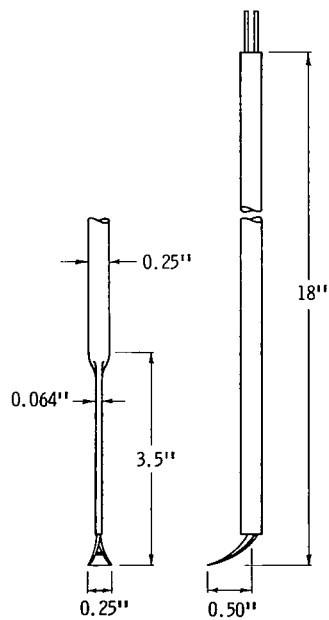
Because of the small boundary-layer thicknesses involved in this experiment, a bare butt-welded chromel-constantan thermocouple, 3 mils in diameter, was used to measure
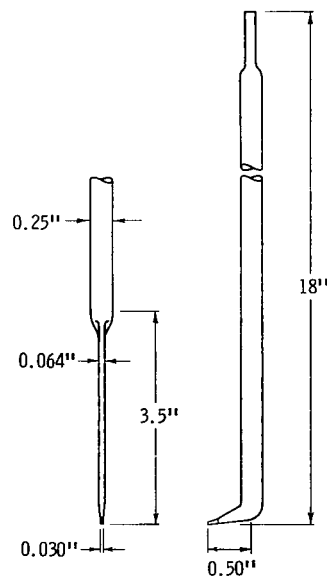
C-66-3024

Thermocouple probe

C-65-2855

Pitot head

0.25"

18"

0.064"

3.5"

0.25"   0.50"

Thermocouple probe

0.25"

18"

0.064"

3.5"

0.030"   0.50"

Pitot tube

CD-8764

Figure 3. - Boundary-layer probes.

the temperature profiles. A diagram of the probe is shown in figure 3 (p. 9). The wire was supported between two prongs, 0.250 inch apart, which were made of 30-mil-diameter thermocouple wire. Epoxy cement was used to insulate the prongs from the smaller wire which was wrapped around the prongs a number of turns to reduce conduction losses. The small wire was welded to the prongs just before entering the stainless-steel probe support. The 30-mil thermocouple lead wire was encased in a plastic insulating sheath inside the probe support. The thermocouple measurement was recorded on a self-balancing potentiometer.

A calibration of the recovery characteristics of the thermocouple probe was obtained over the Mach number range of interest and compared favorably with references 7 and 8. The calibration was conducted at constant static pressure in the same free jet as the pitot-tube calibration for $M = 0$ to 1. Calibration was extended beyond $M = 1$ by use of the free stream of the low gradient test nozzle. A check of the calibration between $M = 0$ and 1 was made in the test nozzle and revealed no differences from the free jet data. A curve faired through the calibration data yielded no deviation from the curve greater than 0.2 percent of the recovery ratio. The recovery ratio, as defined and discussed in reference 8, is

$$R \equiv \frac{T_R}{T_T} \tag{1}$$

where T_R is the temperature measured by the probe and T_T is the local total temperature of the flow. This parameter simplified the data reduction somewhat when compared to the commonly used recovery factor

$$r \equiv \frac{T_R - T}{T_T - T}$$

where T is the static temperature of the flow.

Traversing Devices

A motor driven actuator was used to traverse the boundary layer with either the pitot tube or the thermocouple probe. Position of the probe was indicated by the voltage across a 1.5-inch, 10 500-ohm-carbon-slide wire resistor of infinite resolution. This potentiometer had a linearity of 0.1 percent and was connected directly to the probe so that the play of the actuator gears had no effect on the position measurment. The voltage

source was a voltage stabilized isolated power supply, and the recording mechanism was a digital voltmeter with an accuracy of 0.1 percent of full scale. A full scale reading was 1 volt, and the calibration constant for the linear potentiometer was found to be 0.1248 inch per volt, so that the measuring system could be read to within approximately 0.0001 inch. The calibration constant was found by comparing the measuring system to a dial indicator which could read to within 0.0001 inch.

To determine when either the pitot tube or thermocouple probe was in contact with the cylinder, an electric circuit was formed with the two bodies in series with a battery and a microammeter. One leg of a surface thermocouple acted as the cylinder portion of the circuit.

PROCEDURE AND DATA REDUCTION

Before the velocity profile measurements were made, the static pressure distributions of the nozzles were obtained. The data showed the flows were free of shocks. The measurements were made with and without a boundary-layer probe in position and revealed no indication of instrumentation blockage effects.

To make velocity profile measurements as close as possible to the throat without instrumentation blockage, the pressure profiles and the temperature profiles were measured separately. Since the stagnation conditions were essentially atmospheric pressure and temperature, no difficulty was encountered in reproducing flow conditions between a pitot-tube traverse and a thermocouple probe traverse. Each time a traverse was made, the probe was first contacted with the test cylinder, as indicated by electric continuity, and then moved away until continuity was just broken. This procedure eliminated the possibility of compressing the pitot tube or the thermocouple probe against the cylinder, which would result in false position readings until the compression was relieved. The alinement of the probes relative to the test cylinder was accomplished by observing the reflection of the probe on the mirror-like finish of the test cylinder and by sighting the cylinder and the probe along the centerline of the nozzle. The good reproducibility of the data indicated the alinement procedure was adequate.

After contacting and alining the probe with the test cylinder, the flow was initiated. Before a traverse began, all temperatures were allowed to stabilize. This required about 5 minutes. The boundary-layer probe reading was then recorded, and the traverse began by initially moving the probe about 0.001 inch. The step size of the probe displacement increased as the differences in pressure or temperature between succeeding boundary-layer stations became smaller. A complete traverse generally consisted of about 20 readings of pressure or temperature within a layer 0.125 inch thick over the cylinder. Because of the small size of the boundary-layer probes and the difficulty in

strengthening them without greatly increasing their size, some probe vibration was encountered during the traverse procedure, as noted by the electric contact system. The amplitude of the vibration was estimated to be a few thousandths of an inch using the electric contact system in conjunction with the probe position measuring system. As a result of the pitot-tube vibration, the manometer readings oscillated with an amplitude no greater than 0.05 inch of mercury, which corresponds to a velocity oscillation of no greater than 30 feet per second for this experiment. The average manometer reading was used in the data reduction, and this reading was assumed to correspond to the mean position of the pitot tube. Oscillations of the boundary-layer temperature probe resulted in temperature variations of about 1° F. These variations caused no significant effect on the velocity profiles.

Most of the data reduction procedure was carried out on a digital computer, with boundary-layer velocities calculated according to the following procedure. First, the measured values of static pressure and boundary-layer total pressure were used to calculate a corresponding boundary-layer Mach number by linear interpolation in the compressible flow tables of reference 6. In subsonic flow, the corresponding relation is

$$\frac{P_T}{P} = \left(1 + \frac{\gamma - 1}{2} M^2\right)^{\frac{\gamma}{\gamma - 1}} \qquad (2)$$

for the isentropic flow of a perfect gas. For supersonic flow the normal shock ahead of the pitot-tube mouth is accounted for in reference 6 through the use of the Rayleigh pitot formula

$$\frac{P_{T_2}}{P} = \left[\frac{(\gamma + 1)M^2}{2}\right]^{\frac{\gamma}{\gamma - 1}} \left[\frac{\gamma + 1}{2\gamma M^2 - (\gamma - 1)}\right]^{\frac{1}{\gamma - 1}} \qquad (3)$$

The value of the pressure ratio determined which of the equations applied in calculating the Mach number. As stated in the APPARATUS section, the recovery characteristics of the pitot tubes were calibrated and revealed small differences from the predicted values of pressure ratio over the Mach number range of interest.

From equation (1), the boundary-layer total temperature T_T was calculated using the corresponding Mach number M and the measured recovery temperature T_R. Since the distance of pitot-tube measurements and thermocouple probe measurements from the test cylinder did not correspond, linear interpolation was used to find the value of T_R corresponding to a given pitot-tube measurement. The calibration curve was read into

the computer program as a table, and linear interpolation was used to find the recovery ratio R corresponding to a given M. The boundary-layer static temperature could then be found from the adiabatic, perfect gas relation

$$\frac{T_T}{T} = \left(1 + \frac{\gamma - 1}{2} M^2\right) \tag{4}$$

Since T and M were known, the boundary-layer velocity could be found using the relation

$$u = aM \tag{5}$$

where the sonic velocity

$$a = \sqrt{\gamma \overline{R} T} \tag{6}$$

This calculation procedure for u was carried out for each of the positions corresponding to a pitot-tube measurement.

With a complete set of boundary-layer velocity data, the commonly used boundary thicknesses could be calculated. First, the velocity thickness δ was calculated through linear interpolation. The definition of δ used here is the boundary-layer height where the velocity is equal to 99 percent of the free-stream velocity. The displacement thickness, a measurement of the mass flux defect, was calculated from the relation

$$\delta^* \equiv \int_0^\infty \left(1 - \frac{\rho u}{\rho_e u_e}\right) dy = \int_0^\infty \left(1 - \frac{T_e u}{T u_e}\right) dy \tag{7}$$

where density and temperature are related by the perfect gas law

$$P = \rho \overline{R} T \tag{8}$$

The upper limit in the numerical integration of equation (7) was the last data point of the pitot-tube survey, which was well outside the boundary layer. The momentum thickness was calculated from the relation

13

$$\theta \equiv \int_0^\infty \frac{\rho u}{\rho_e u_e}\left(1 - \frac{u}{u_e}\right)dy = \int_0^\infty \frac{T_e u}{T u_e}\left(1 - \frac{u}{u_e}\right)dy \tag{9}$$

where the same integration procedure was used as for equation (7). The numerical integration technique used was a computer subroutine, which uses a spline fit of the data points. A number of calculations were hand checked, and no differences greater than 5 percent existed between the machine and the hand computations.

RESULTS AND DISCUSSION

The velocity profile data are presented on a dimensionless basis in figures 4 to 11 to facilitate comparison with power profiles of the form

$$\frac{u}{u_e} = \left(\frac{y}{\delta}\right)^{1/n} \tag{10}$$

(a) Rectangular coordinates. $(D_t/P_0)(dP/dx) = -0.27$, where D_t is throat diameter, P is pressure, and x is axial distance.

(b) Logarithmic coordinates. Denominator of exponent in velocity power law n, 2.1.
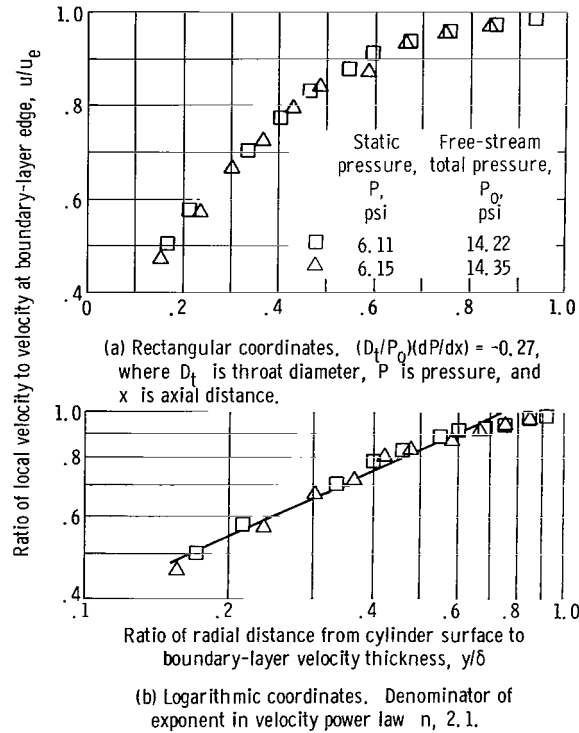
Figure 4. – Velocity profile for low-gradient nozzle, short cylinder. Free-stream total temperature, 546° R.

14

Static pressure, P, psi	Free-stream total pressure, P_0, psi	Free-stream total temperature, T_0, °R
○ 6.18	14.26	542
□ 6.16	14.33	541
△ 6.14	14.30	542

(a) Rectangular coordinates. $(D_t/P_0)(dP/dx) = -0.27$, where D_t is throat diameter, P is pressure, and x is axial distance.

(b) Logarithmic coordinates. Denominator of exponent in velocity power law n, 6.8.
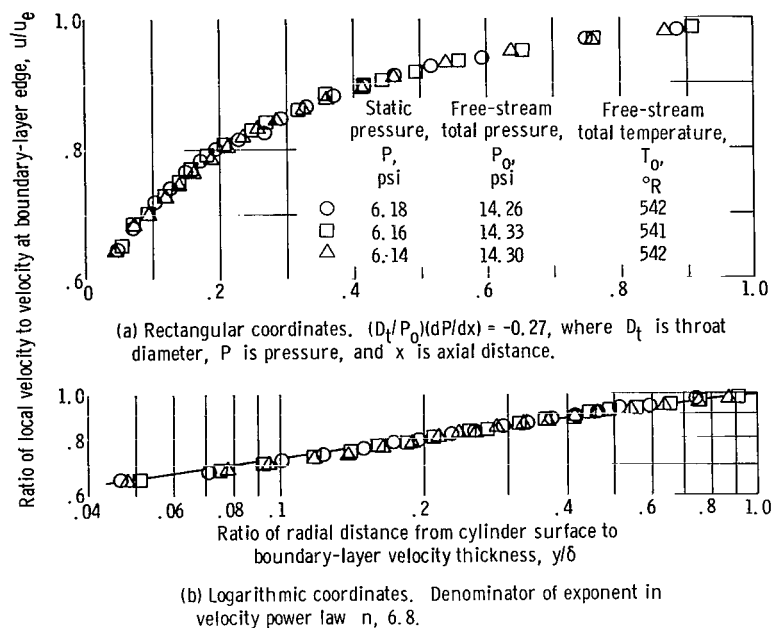
Figure 5. - Velocity profile for low-gradient nozzle, short cylinder with trip.

Part (a) of each figure shows the data as commonly presented in rectangular coordinates, while part (b) shows the data on logarithmic scales so that the parameter n of equation (10) can be examined. At least two test runs were made with each flow configuration and the data presented are typical for the configuration. Enough data are shown to estimate the scatter involved with the experiment. Given with each figure are the free-stream stagnation pressure and temperature, the wall static pressure (assumed equal to the free-stream value), and a static pressure gradient parameter, which has been made dimensionless by multiplying the gradient dP/dx by the ratio of the nozzle-throat diameter to the free-stream stagnation pressure. An equivalent throat diameter, four times the cross-sectional area of flow divided by the wetted perimeter, was used in this parameter. No theoretical basis for using this particular pressure gradient parameter exists, but no parameter has been commonly accepted in the literature at this time to compare experiments. Enough data is presented, however, to compare the pressure gradients in any manner which may be desired.

Probe Effects

As previously stated, three sizes of pitot-tube mouths were used. The comparative results are shown in figures 6, 7, and 9. The remaining data were measured with pitot tubes having a height of 2 mils. No significant differences are indicated in figure 6.
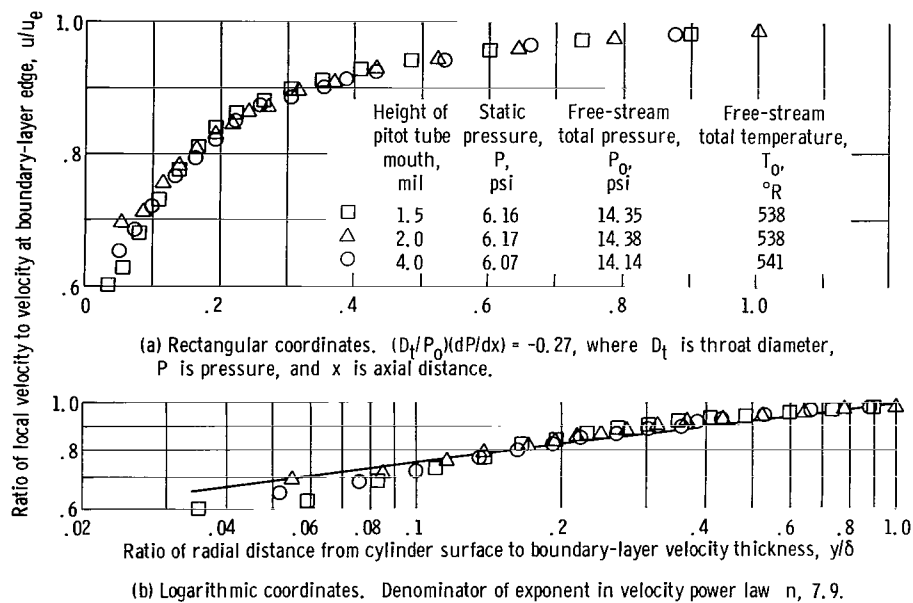
	Height of pitot tube mouth, mil	Static pressure, P, psi	Free-stream total pressure, P_0, psi	Free-stream total temperature, T_0, °R
□	1.5	6.16	14.35	538
△	2.0	6.17	14.38	538
○	4.0	6.07	14.14	541

(a) Rectangular coordinates. $(D_t/P_0)(dP/dx) = -0.27$, where D_t is throat diameter, P is pressure, and x is axial distance.

(b) Logarithmic coordinates. Denominator of exponent in velocity power law n, 7.9.

Figure 6. – Velocity profile for low-gradient nozzle, long cylinder.

	Probe, mil	Static pressure, P, psi	Free-stream total pressure, P_0, psi	Free-stream total temperature, T_0, °R
△	1.5	6.15	14.31	540
□	2.0	6.13	14.30	538
○	4.0	6.16	14.35	538

(a) Rectangular coordinates. $(D_t/P_0)(dP/dx) = -0.27$, where D_t is throat diameter, P is pressure, and x is axial distance.

(b) Logarithmic coordinates. Denominator of exponent in velocity power law n, 8.0.
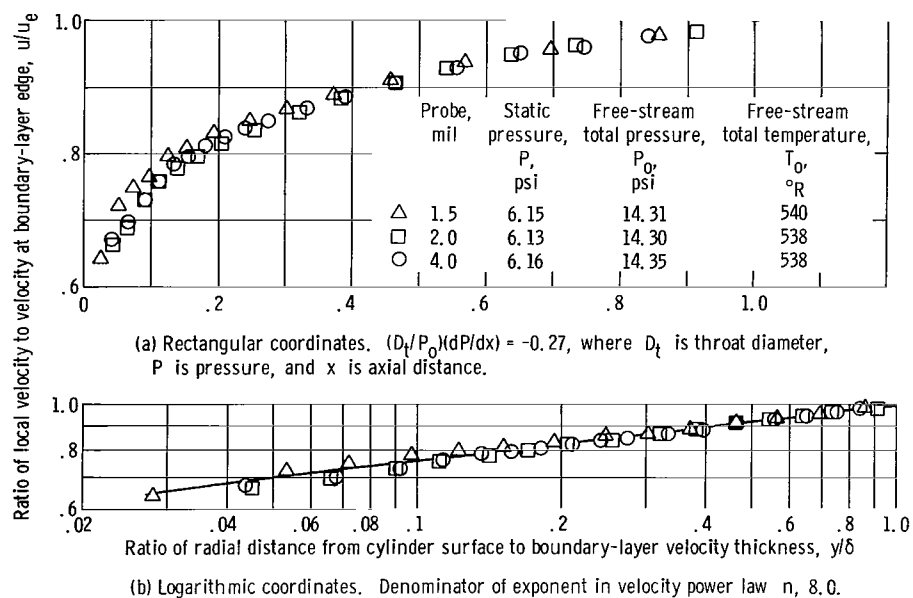
Figure 7. – Velocity profile for low-gradient nozzle, long cylinder with trip.

16

(a) Rectangular coordinates. $(D_t/P_0)(dP/dx) = -0.76$, where D_t is throat diameter, P is pressure, and x is axial distance.

(b) Logarithmic coordinates. Denominator of exponent in velocity power law n, 6.4.
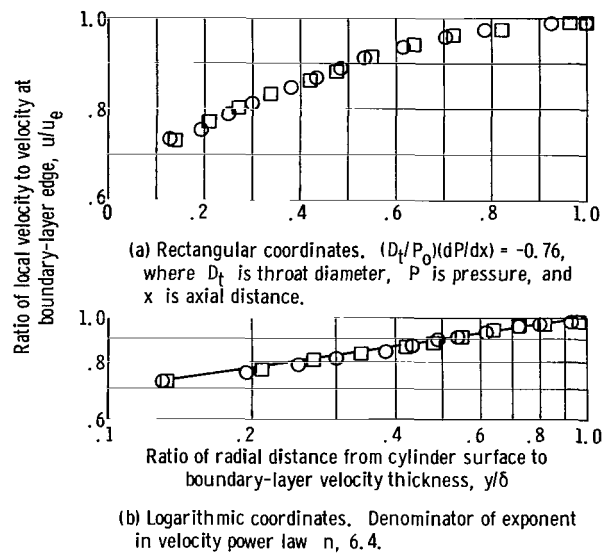
Figure 8. - Velocity profile for high-gradient nozzle, short cylinder. Static pressure, 6.88 psi; free-stream total pressure, 14.36 psi; free-stream total temperature, 532° R.

Probe, mil	Static pressure, P, psi	Free-stream total pressure, P_0, psi
O 4	6.89	14.38
□ 4	6.85	14.31
△ 2	6.91	14.44

(a) Rectangular coordinates. $(D_t/P_0)(dP/dx) = -0.76$, where D_t is throat diameter, P is pressure, and x is axial distance.

(b) Logarithmic coordinates. Denominator of exponent in velocity power law n, 10.5.
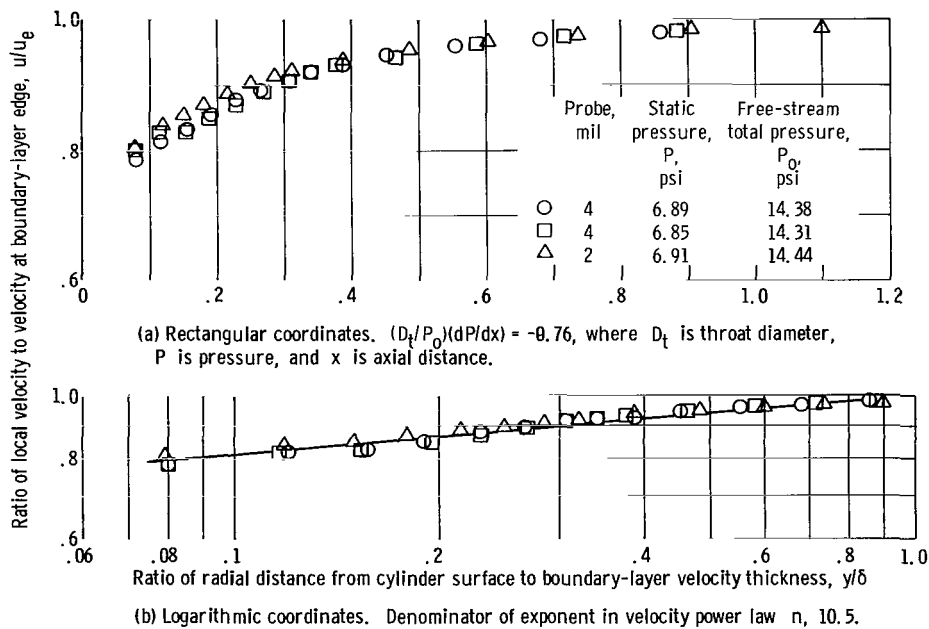
Figure 9. - Velocity profile for high-gradient nozzle, short cylinder with trip. Free-stream total temperature, 532° R.

The data of figure 7 indicate differences as great as 6 percent in velocity ratio at a given distance between the 1.5-mil probe and the other two probes on the inner portion of the profile. Figure 9 compares measurements with 2 mil and 4 mil probes only, and indicates a 2-percent maximum difference on the inner portion of the profile. In both cases where differences are indicated, the smaller pitot tubes indicate a higher total pressure or higher velocity than the larger pitot tubes. This is opposite to the predictions of references 9 and 10. The ratio of pitot-tube height to boundary-layer thickness for each probe is well below the critical value of 0.29 given in reference 11, which quotes other sources on this value. All probes with height-to-thickness ratios below this value are expected to record the same total pressure profile. If this is true, then the differences in velocity measurements between the probes cannot be entirely attributed to geometry effects.

Another possible cause for the differences in pitot-tube reading was the vibration mentioned in the PROCEDURE AND DATA REDUCTION section, which effectively destroyed the 0.0001-inch position accuracy estimated by the potentiometer calibration. Differences between velocity profiles where only 2-mil pitot tubes were used can also be observed and are about the same size as the differences obtained with the other geometries. The magnitude of the error can be measured by examining the maximum displacement between individual profiles, which is about 2 mils. The vibration problem was more likely the cause of the differences than any error due to geometry effects or any other source, such as manometer accuracy.

Velocity Power Profiles and Thickness Parameters

The velocity power law (eq. (10)) originated with the Blasius resistance formula for pipes (ref. 12) and was found to be transferable to channel flow and flat plate boundary-layer flow. The value of the parameter n is generally used to classify the flow regime with $n = 2$ associated with laminar flow and $n = 7$ associated with turbulent flow for Reynolds numbers based on boundary-layer velocity thickness Re_δ below 100 000. Above this value of Re_δ, values of $n = 8$ or 9 have been used (ref. 12). Lacking boundary-layer velocity measurements taken under the proper conditions, rocket-nozzle heat-transfer analysts (refs. 1 and 4) have continued to use the empirical power law relations with generally a value of $n = 7$. As stated in reference 4, this value could affect the thickness parameters and in turn, the friction law and Reynolds analogy between heat and momentum used in integral prediction methods such as reference 1.

The values of n for this experiment varied between 2.1 and 11.0 and are presented with the appropriate logarithmic velocity profile and also in table II. The value $n = 2.1$, which indicates a laminar-like profile, was measured with the short test cylinder in the

TABLE II. - SUMMARY OF BOUNDARY LAYER PARAMETERS

[Equivalent throat diameter, D_t, 3.80 in.; free-stream total pressure, P_o, 14.3 psi.]

	Low-gradient nozzle (a)				High-gradient nozzle (b)			
	Short cylinder		Long cylinder		Short cylinder		Long cylinder	
	No trip	Trip	No trip	Trip	No trip	Trip	No trip	Trip
Boundary-layer thickness, δ, in.	18.6×10^{-3}	62.0×10^{-3}	57.0×10^{-3}	69.0×10^{-3}	22.3×10^{-3}	37.7×10^{-3}	30.4×10^{-3}	49.0×10^{-3}
Displacement thickness, δ^*, in.	5.7×10^{-3}	10.2×10^{-3}	8.0×10^{-3}	10.7×10^{-3}	4.5×10^{-3}	4.6×10^{-3}	4.9×10^{-3}	6.0×10^{-3}
Momentum thickness, θ, in.	2.0×10^{-3}	5.1×10^{-3}	4.0×10^{-3}	5.5×10^{-3}	2.0×10^{-3}	2.2×10^{-3}	2.2×10^{-3}	3.0×10^{-3}
Reynolds number, ft^{-1}	4.42×10^{6}	4.44×10^{6}	4.41×10^{6}	4.45×10^{6}	4.47×10^{6}	4.46×10^{6}	4.45×10^{6}	4.44×10^{6}
Denominator of exponent in velocity-power law, n	2.1	6.8	7.9	8.0	6.4	10.5	8.0	11.0
Friction coefficient, C_f	0.60×10^{-3}	3.26×10^{-3}	3.58×10^{-3}	3.29×10^{-3}	4.52×10^{-3}	4.39×10^{-3}	4.37×10^{-3}	4.18×10^{-3}

[a]$(D_t/P_o)(dP/dx) = -0.27$; $M_e = 1.17$.
[b]$(D_t/P_o)(dP/dx) = -0.76$; $M_e = 1.08$.

low-gradient nozzle where the boundary layer was not tripped. Although no attempt was made to obtain laminar flow, the results of figure 4 (p. 14) are not surprising. Reference 13 states that transition from laminar flow begins at about a value of 645 for the Reynolds number based on displacement thickness Re_{δ^*}, where zero pressure gradient exists. However, with favorable pressure gradients (decreasing static pressure in the flow direction), which have a large stabilizing effect on laminar boundary layers, this value is increased significantly. Since the Reynolds number Re_{δ^*} corresponding to the data of figure 4 was about 2400, which is within the range of critical values given in reference 13, the laminar-like profile is not unreasonable. The other flow configurations had Reynolds numbers in the same range, but the corresponding boundary layers must be considered nonlaminar in general and definitely turbulent in most cases as indicated by the turbulent-like values for n. A boundary-layer stability investigation was beyond the scope of this experiment, and, thus, no further attempt will be made to explain the results on this basis.

Comparisons of figure 4 (p. 14) to figure 6 (p. 16) and of figure 5 (p. 15) to figure 7 (p. 16) for the low-gradient nozzle and similar comparisons for the high-gradient nozzle reveal that increased development length caused a flattening of the velocity profiles which is indicated by increased values for n. A corresponding increase in n due to boundary-layer tripping can also be observed by comparing the appropriate figures (e. g. , fig. 4 to fig. 5). By comparing like-flow configurations for the two nozzles (e. g. , fig. 4 to fig. 8), higher values of n are indicated for the high-gradient nozzle. In summary, the
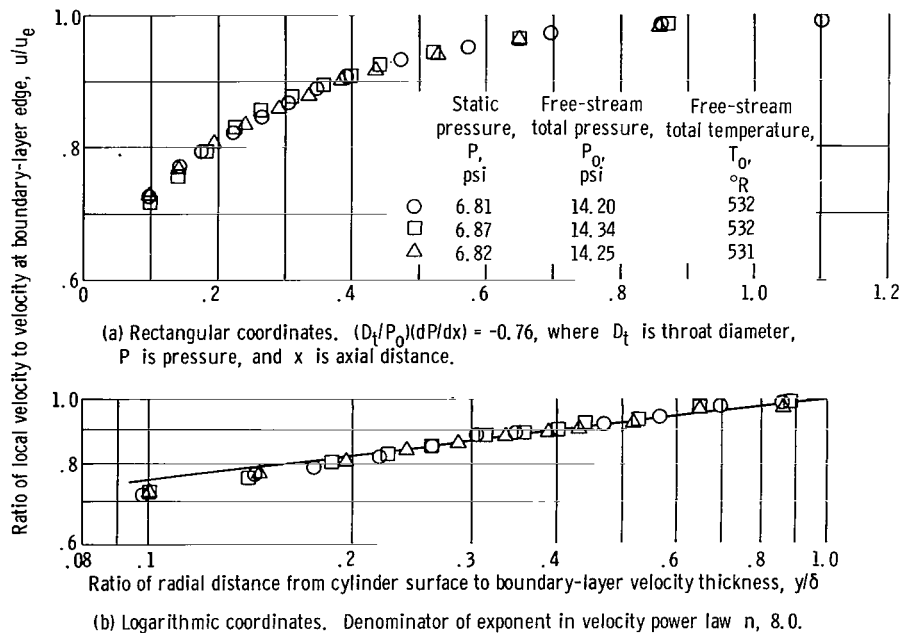

(a) Rectangular coordinates. $(D_t/P_0)(dP/dx) = -0.76$, where D_t is throat diameter, P is pressure, and x is axial distance.

(b) Logarithmic coordinates. Denominator of exponent in velocity power law n, 8.0.

Figure 10. - Velocity profile for high-gradient nozzle, long cylinder.

Ratio of local velocity to velocity at boundary-layer edge, u/u_e

1.0

.8

.6

Static pressure, P, psi	Free-stream total pressure, P_0, psi
○ 6.87	14.36
□ 6.89	14.35
△ 6.81	14.21

0 .2 .4 .6 .8 1.0

(a) Rectangular coordinates. $(D_t/P_0)(dP/dx) = -0.76$, where D_t is throat diameter, P is pressure, and x is axial distance.

1.0
.8
.6

.04 .06 .08 .1 .2 .4 .6 .8 1.0

Ratio of radial distance from cylinder surface to boundary-layer velocity thickness, y/δ

(b) Logarithmic coordinates. Denominator of exponent in velocity power law n, 11.0.

Figure 11. - Velocity profile for high-gradient nozzle, long cylinder with trip. Free-stream total temperature, 536° R.

velocity profiles were flattened, as indicated by increased n, when development length was increased, when the boundary layer was tripped, and when the pressure gradient was made more favorable. Boundary-layer history effects, development length, and tripping were not believed to be greatly affected by the acceleration histories of the two nozzles. This conclusion is indicated again by the different values for n corresponding to the different test cylinder configurations.

A summary of average values for the boundary-layer thicknesses, the values of n (eq. (10)), and unit Reynolds numbers (based on 1-ft length) is given in table II (p. 19). As expected, the various boundary-layer thicknesses increased with tripping and increased development length. Except for the case of the short cylinder with no trip, the thickness quantities for the low-gradient nozzle were larger than those of the high-gradient nozzle. This result is attributed to the different pressure or acceleration histories of the flows in the two nozzles.

Universal Profiles

In figures 12 to 18 (pp. 22 to 25, respectively) the turbulent-like velocity profiles of the present experiment are compared to two forms of the "law of the wall" (ref. 12) and
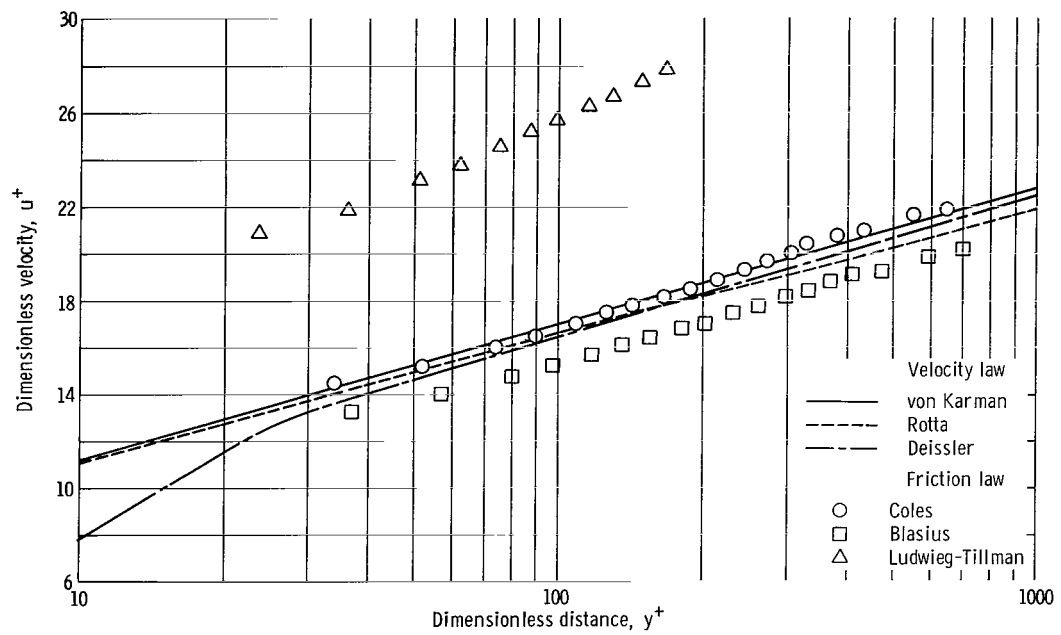
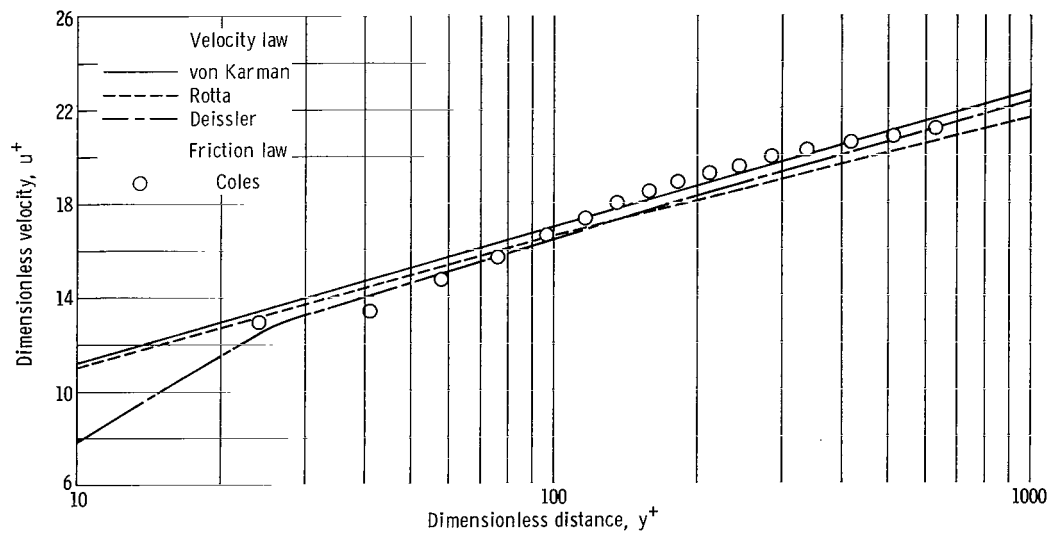Figure 12. - Velocity profile for low-gradient nozzle, short cylinder with trip.

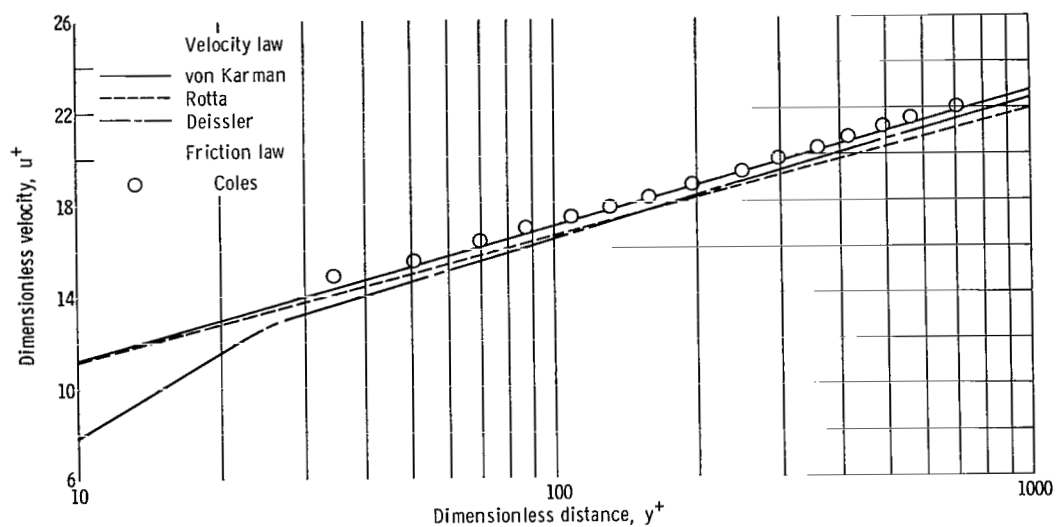Figure 13. - Velocity profile for low-gradient nozzle, long cylinder.

22

Figure 14. - Velocity profile for low-gradient nozzle, long cylinder with trip.
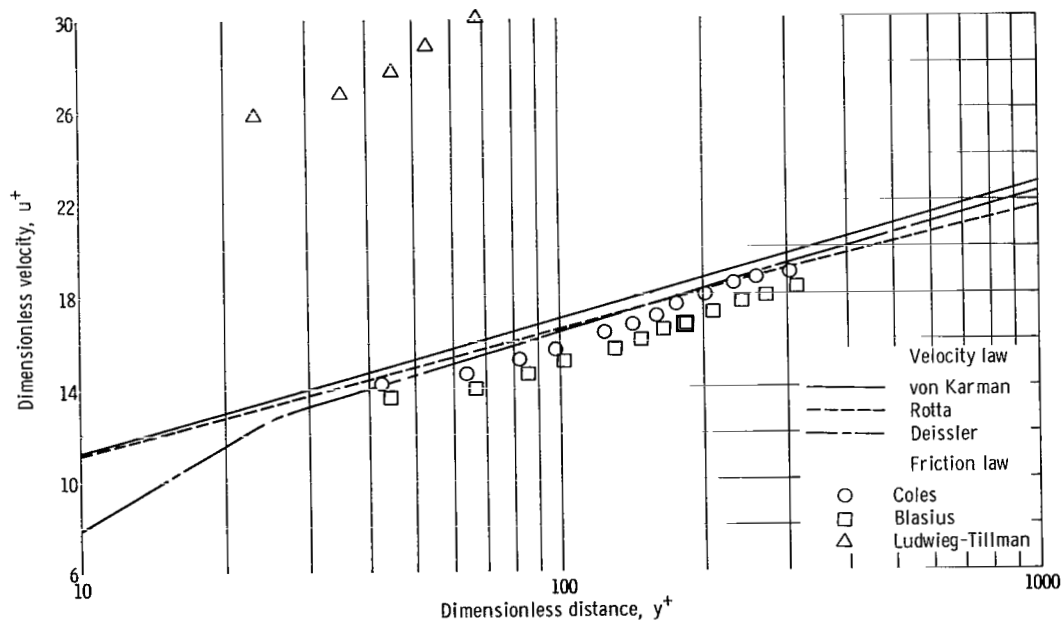

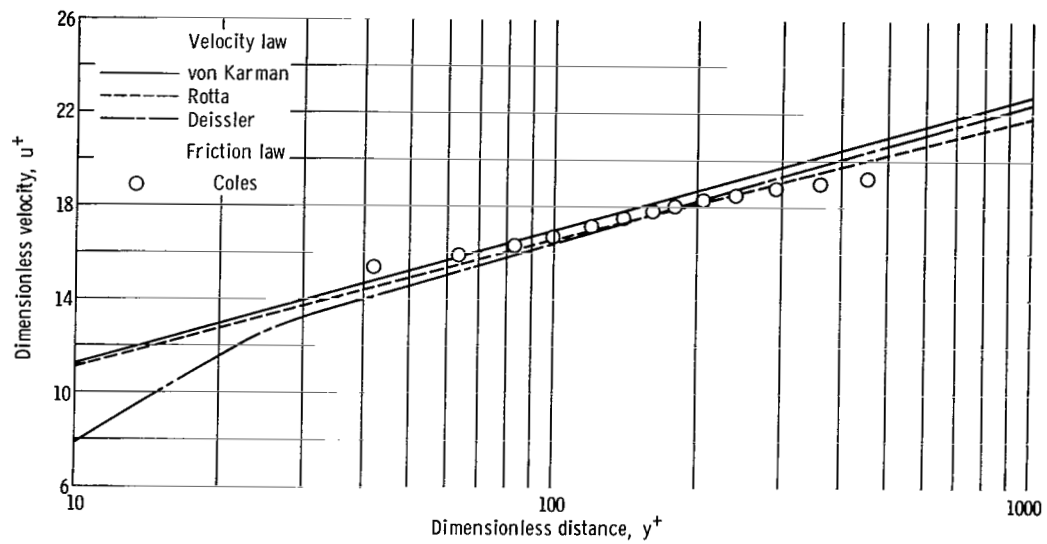Figure 15. - Velocity profile for high-gradient nozzle, short cylinder.

23

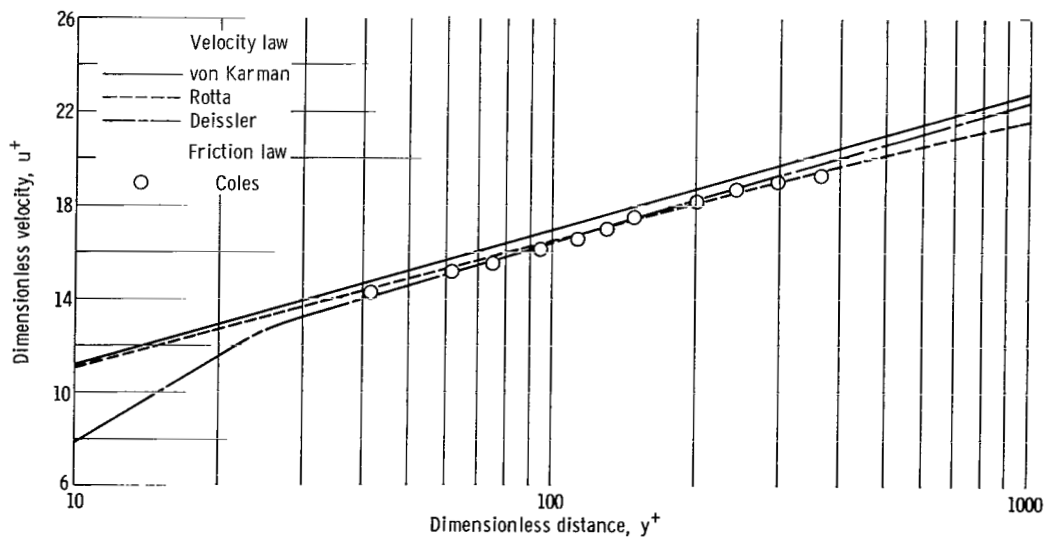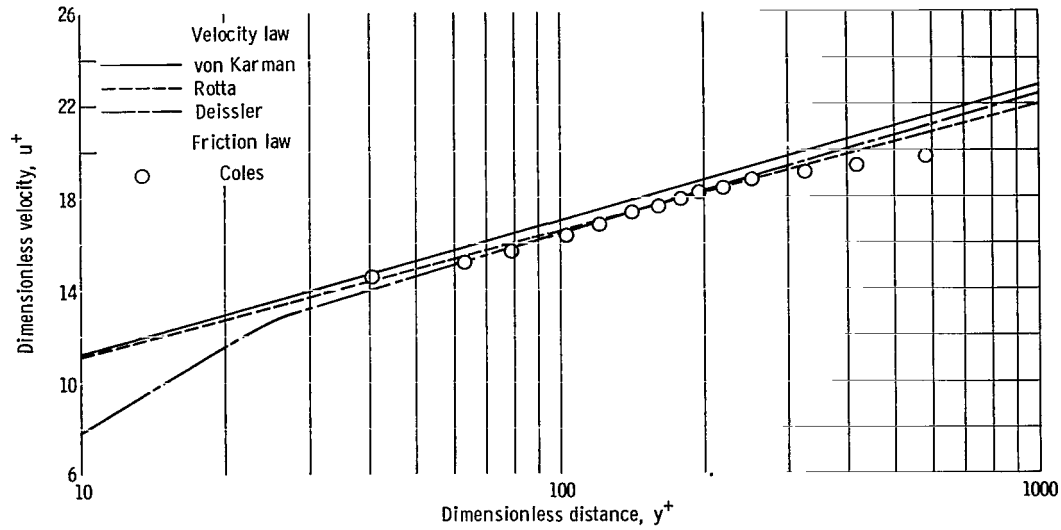Figure 16. - Velocity profile for high-gradient nozzle, short cylinder with trip.

Figure 17. - Velocity profile for high-gradient nozzle, long cylinder.

24

Figure 18. - Velocity profile for high-gradient nozzle, long cylinder with trip.

the differential type analysis of Deissler (ref. 14). The profiles were made dimension-less by using the definitions

$$y^+ \equiv \frac{y \sqrt{\dfrac{\tau_w}{\rho_w}}}{\dfrac{\mu_w}{\rho_w}} \tag{11}$$

$$u^+ \equiv \frac{u}{\sqrt{\dfrac{\tau_w}{\rho_w}}} \tag{12}$$

where

$$\tau_w \equiv \frac{C_f}{2} \rho_e u_e^2 \tag{13}$$

After a comparison of a number of friction laws, the best relation for the friction coefficient C_f was found to be that of Coles (ref. 1), which employs a compressible transformation method to give C_f as a function of the Mach number and the momentum thickness Reynolds number. Essentially, Coles showed that the available data on C_f

25

could be correlated within a few percent by a single curve of $\overline{C}_f = \overline{C}_f(C_f)$ as a function of $\overline{C}_f \overline{Re}_\theta = \overline{C}_f \overline{Re}_\theta (C_f Re_\theta)$ where the "barred" quantities are the values of C_f and Re_θ for low-speed flow. Reference 1 should be consulted for a detailed description of the iterative procedure required to find C_f.

As shown in figures 12 to 18 (pp. 22 to 25, respectively), the use of Coles C_f causes the data of the present experiment to agree fairly well with the three theoretical velocity profiles considered. The von Karman "law of the wall" relation

$$u^+ = 5.5 + 2.5 \ln y^+ \tag{14}$$

is for incompressible flow with zero pressure gradient, and the other two relations are for compressible flow with zero pressure gradient. Rotta's distribution can be written for adiabatic flow as (ref. 15)

$$u^+ = \frac{\sqrt{C_1}}{\sqrt{\sigma_t \frac{\gamma - 1}{2} M_\tau}} \sin \left[\sqrt{\sigma_t \frac{\gamma - 1}{2}} M_\tau \left(2.5 \ln y^+ + C_2 \right) \right] \tag{15}$$

where

$$C_1 = 1 - 0.2 M_\tau$$

$$C_2 = 5.2 + 5 M_\tau$$

$$M_\tau \equiv \sqrt{\frac{\tau_w}{\gamma P}}$$

The turbulent Prandtl number σ_t is taken as 0.9 and the wall friction was evaluated with Coles relation. The use of the von Karman and the Rotta relations was suggested by references 2 and 3, respectively, where good results were obtained with them. The Deissler analysis does not have an explicit relation like equations (14) and (15), but must be solved numerically (ref. 14). The wide departure of this relation from the other two at about $y^+ = 26$ is due to consideration of varying eddy diffusivity.

In figures 12 and 15 (pp. 22 and 23, respectively), results of the friction law comparisons used to determine the best relation for C_f are indicated. The Blasius and the Ludwieg-Tillman friction relations are used to present the data on a dimensionless basis along with the Coles relation. The Deissler and the Rotta theoretical curves, which are weak functions of C_f, are shown only as evaluated with Coles C_f, since the other rela-

tions moved the curves only slightly. The Blasius relation (ref. 13)

$$\frac{C_f}{2} = 0.0128 \left(\frac{\rho_e u_e \theta}{\mu_e}\right)^{-1/4} \tag{16}$$

was used with good results in reference 2, but was originally intended for incompressible flow with zero pressure gradient. The Ludweig-Tillman relation (ref. 12)

$$\frac{C_f}{2} = \frac{0.123}{10^{0.678 \, \delta^*/\theta} \, Re_\theta^{0.268}} \tag{17}$$

has won some acceptance as the proper relation for flows with pressure gradient, but for the present experiment yielded very poor results. Although the Coles relation yielded better results than equations (16) and (17) for this experiment, it should not be construed that it will always yield such good results. Figures 12 and 15 indicate that further work is necessary in the area of turbulent skin friction.

Considering the lack of knowledge about the actual friction in this experiment, the data compared favorably to the theoretical relations. In the y^+ region of interest the theoretical curves are generally linear, while the data has an "extended-S" shape, which is typical of turbulent velocity profiles presented on this basis (refs. 12 and 14). No significant effects of development length, tripping, or pressure gradient were noted in the comparison of data and theory. Also, no conclusion could be reached as to which theoretical relation is best because of the nature of the data which generally spread over the narrow region bounded by the theoretical curves.

A summary of the Coles friction coefficients used to obtain figures 12 to 18 is presented in table II (p. 19) along with a C_f value for the laminar-like profile of figure 4 (p. 14). The laminar C_f was calculated from the Blasius solution to the incompressible laminar boundary-layer equation (ref. 13). Considering the values of C_f for the turbulent-like profiles only, the high-gradient nozzle coefficients show an average increase of 29 percent over the corresponding values for the test cylinder configurations in the low-gradient nozzle. This increase occurred even though the unit Reynolds numbers (and thus, $\rho_e u_e$) for all the tests varied only about 1 percent. The large difference in C_f between nozzles can be attributed to the different pressure histories involved and the resulting effect on the momentum thickness Reynolds numbers Re_θ. If any heat transfer had occurred in this experiment, a corresponding large difference in Stanton number would be expected between the high- and the low-gradient nozzle tests, since the

Stanton number and the friction coefficient can be related through some form of Reynolds analogy (refs. 1 and 13).

Temperature Profiles

The normal procedure for adiabatic velocity profile measurements is to assume the total temperature constant through the boundary layer, and this assumption was confirmed by measuring the boundary-layer temperature profiles in this experiment. The temperature distributions corresponding to the data of the low-gradient nozzle, short cylinder with trip flow configuration are presented in figure 19 to indicate the flatness of the total temperature profile. When the measured recovery temperature distribution was used to calculate the total temperature distribution, the velocity corresponding to the innermost pitot measurement was found to be 768 feet per second. If the total temperature had been assumed equal to the free-stream value throughout the boundary layer, the calculated velocity would have been 770 feet per second, differing 0.3 percent from the actual value. The temperature distributions for the other flow configurations are very similar to those of figure 19 and are not presented.
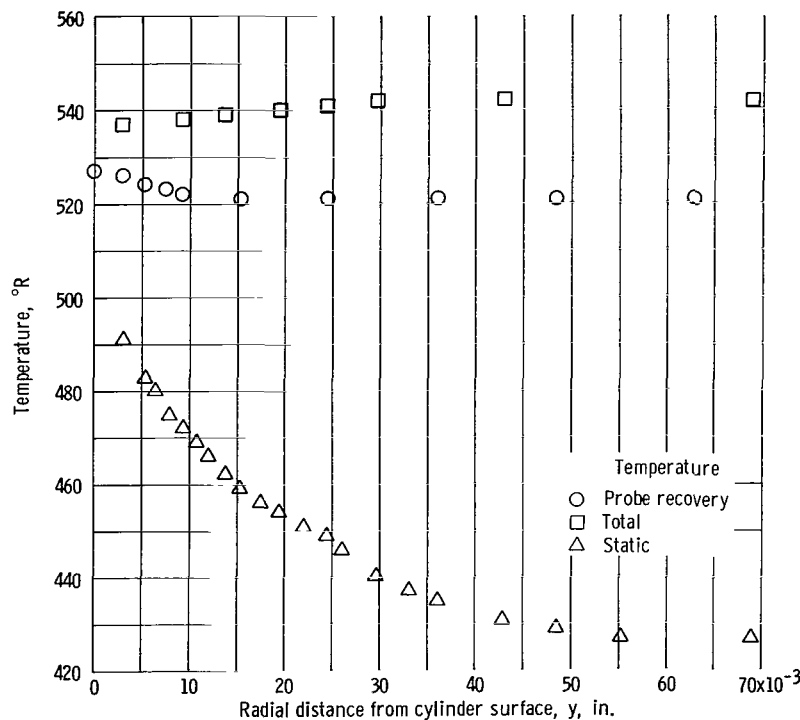

Figure 19. - Temperature profiles for low-gradient nozzle, short cylinder with trip.
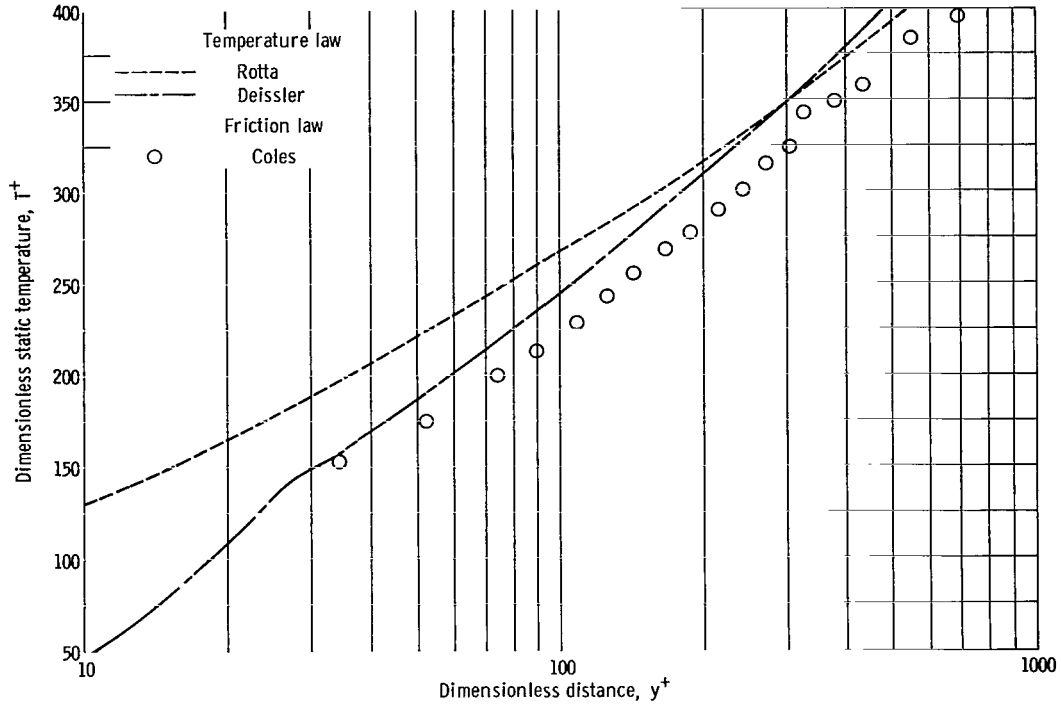
Figure 20. – Static temperature profile for low-gradient nozzle, short cylinder with trip.

The static temperature data of figure 19 are presented on a dimensionless basis in figure 20 where

$$T^+ \equiv \frac{4\left(1 - \dfrac{T}{T_w}\right)}{C_f(\gamma - 1)M_e^2} \tag{18}$$

The data are compared with the theoretical relations of Deissler (ref. 14) and Rotta (ref. 15) using Coles friction law for C_f (ref. 1). Rotta's relation can be written

$$T^+ = \frac{2(1 - C_1)}{(\gamma - 1)M_\tau^2} + \sigma_t u^{+2} \tag{19}$$

where C_1, M_τ, and σ_t were previously defined with the relation for $u^+ = u^+(y^+)$. A numerical integration is required for Deissler's analysis of T^+, and no explicit relation is possible. The agreement of the data and the theory is not good when compared to the generally good agreement of the velocity data (figs. 12 to 18, pp. 22 to 25, respectively)

with theory. However, this lack of agreement is not surprising since, from equations (5), (6), and (19), the static temperature is shown to be a function of the velocity squared.

Comparison to Similar Experiments

As stated in the INTRODUCTION section, references 2 and 3 reported velocity profile measurements taken under mild favorable pressure gradient conditions. The results of these two reports should be comparable to the data of the present report since the measurements were made with approximately the same stagnation conditions and in the transonic flow regime. In reference 2, the gradient varied over the approximate range $(D_t/P_o)(dP/dx) = -0.1$ to -0.2, and the exponent n of equation (10) varied between 7.0 and 7.5. The von Karman universal profile (eq. (14)) used with the Blasius C_f (eq. (16)) approximated the measured data well. In reference 3, the pressure gradient examined was about $(D_t/P_o)(dP/dx) = -0.03$, and the corresponding value of n was approximately 10. The boundary-layer velocity thicknesses of reference 3, measured on the convex section of the center body, were the same order of magnitude as the center body diameter, which resulted in static pressure gradients normal to the flow direction. An apparent increase in n could result since the acceleration over the shoulder of the body would cause lower pressures close to the body than existed in the free stream and corresponding flattening of the boundary-layer velocity profile. The Rotta universal profile (eq. (15)) used with an incompressible friction law (ref. 3) approximated this data fairly well. In summary, the data of the present experiment, measured with the two gradients $(D_t/P_o)(dP/dx) = -0.27$ and -0.76, yielded a range of $n = 2.1$ to 11.0 and correlated well with the theories of von Karman, Rotta, and Deissler used with Coles C_f.

The summary of the results of the above three experiments suggests the possibility of using selected available prediction techniques to approximate boundary-layer velocity profiles with favorable pressure gradients and mild curvature of the flow. This last condition is due to the nature of the experiments of references 2 and 3. The data of reference 4, however, most definitely indicate an unusual velocity profile in the convergent section of the nozzle which developed from a standard 1/7-power profile in the cylindrical inlet and which could not be correlated with any standard theory. This very flat profile, of the order of 1/20 or 1/30 power, was measured at about $M_e = 0.08$ with a pressure gradient $(D_t/P_o)(dP/dx) = -0.013$. The stagnation pressure was 300 pounds per square inch absolute. The same results were obtained when the air was heated to 500° F, and the nozzle was cooled as when adiabatic measurements were made. The high value of n measured in reference 4 indicates an acceleration effect on the velocity profile. As explained in the report, the differences between the measured integral quantities, such as θ and δ^*, and those predicted by reference 1 could affect the accuracy of the

heat-transfer quantities predicted by reference 1.

Considering the results of the present experiment, along with references 2 and 3, it does seem reasonable to expect normal (n = 7 to 10) turbulent velocity profiles at the throat of a nozzle similar to that of reference 4 if pressure history is judged to be the governing factor in boundary-layer development. This conclusion is believed true because the throat gradient of reference 4 was only about 30 percent more favorable than that for the high-gradient nozzle examined here. The pressure gradient parameter used here, however, may not be proper for comparing experiments, and other effects, such as heat transfer or wall curvature, may be more important in boundary-layer development than pressure history. More research in the area of acceleration effects on boundary-layer development does seem necessary.

SUMMARY OF RESULTS

Experimental velocity and temperature profiles for the adiabatic boundary layers on cylindrical bodies in parallel accelerated flows have been presented. The measurements were made near Mach 1 with the accelerations imposed by two axisymmetric nozzles having large differences in pressure gradient. Boundary-layer history effects were also examined. The following results were indicated:

1. An attempt to correlate the velocity profiles on the basis

$$\frac{u}{u_e} = \left(\frac{y}{\delta}\right)^{1/n}$$

yielded a range of values for n between 2.1 and 11.0, where u is velocity, u_e is velocity at boundary-layer edge, y is radial distance from cylinder surface, and δ is boundary layer velocity thickness. In general, the tests run in the nozzle having the more favorable pressure gradient yielded higher values for n, and boundary-layer tripping and increased development length also increased n.

2. The turbulent velocity profiles compared favorably with the von Karman and the Rotta forms for the "law of the wall" and the Deissler method of prediction (NASA Technical Report R-17). Coles friction law was found to give the best agreement between these theories and the data.

3. The friction coefficients for the test cylinders in the nozzle having the more favorable pressure gradient were significantly higher than those for the other nozzle. Through Reynolds analogy, a similar effect on heat transfer in a nonadiabatic flow field could be anticipated.

4. The measured temperature profiles did not compare well with the theories of Rotta or Deissler, but the total temperature profiles calculated from the measured recovery temperature profiles confirmed the common assumption of constant total temperature for adiabatic boundary-layer flow.

Lewis Research Center,
    National Aeronautics and Space Administration,
        Cleveland, Ohio, November 1, 1966,
            129-01-09-06-22.

REFERENCES

1. Elliot, David G.; Bartz, Donald R.; and Silver, Sidney: Calculation of Turbulent Boundary-Layer Growth and Heat Transfer in Axi-Symmetric Nozzles. Rep. No. 32-387, Jet Propulsion Lab., Calif. Inst. Tech., Feb. 1963.

2. Sibulkin, Merwin: Boundary-Layer Measurements at Supersonic Nozzle Throats. Rep. No. 20-97, Jet Propulsion Lab., Calif. Inst. Tech., May 1, 1956.

3. Clutter, Darwin W.; and Kaups, Kalle: Wind-Tunnel Investigation of Turbulent Boundary Layers on Axially Symmetric Bodies at Supersonic Speeds. Rept. No. LB31425, Douglas Aircraft Co., Inc., Feb. 1964. (Available from DDC as AD-435111.)

4. Boldman, Donald R.; Schmidt, James F.; and Fortini, Anthony: Turbulence, Heat-Transfer, and Boundary Layer Measurements in a Conical Nozzle With a Controlled Inlet Velocity Profile. NASA TN D-3221, 1966.

5. Burgess, Warren C., Jr.; and Seashore, Ferris L.: Criterions for Condensation-Free Flow in Supersonic Tunnels. NACA TN 2518, 1951.

6. Ames Research Staff: Equations, Tables, and Charts for Compressible Flow. NACA TR 1135, 1953.

7. Simmons, Frederick S.: Recovery Corrections for Butt-Welded, Straight-Wire Thermocouples in High Velocity, High Temperature Gas Streams. NACA RM E54G22a, 1954.

8. Stickney, Truman M.: Recovery and Time-Response Characteristics of Six Thermocouple Probes in Subsonic and Supersonic Flows. NACA TN 3455, 1955.

9. Marson, G. B.; and Lilley, G. M.: The Displacement Effect of Pitot Tubes in Narrow Wakes at Subsonic and Supersonic Speeds. Rept. No. 107, The College of Aeronautics, Cranfield, Gt. Brit., Oct. 1956.

10. MacMillan, F. A.: Experiments on Pitot-Tubes in Shear Flow. R&M No. 3028, British A.R.C., 1957.

11. Galezowski, Stanley H.: Effects of Probe Tip Geometry and Size on Measurements in a Laminar Boundary Layer in Supersonic Flow. Tech. Note No. 17, Inst. of Aerophysics, University of Toronto, Oct. 1957.

12. Schubauer, G. B.; and Tchen, C. M.: Turbulent Flow. Turbulent Flows and Heat Transfer. Vol. 5 of High Speed Aerodynamics and Jet Propulsion, C. C. Lin, ed., Princeton University Press, 1959, pp. 75-195.

13. Schlichting, Hermann (J. Kestin, trans.): Boundary Layer Theory. McGraw-Hill Book Co., Inc., 1955.

14. Deissler, R. G.; and Loeffler, A. L.: Analysis of Turbulent Flow and Heat Transfer on a Flat Plate at High Mach Numbers with Variable Fluid Properties. NASA TR R-17, 1959.

15. Rotta, J. C.: Turbulent Boundary Layers with Heat Transfer in Compressible Flow. AGARD Rep. No. 281, Apr. 1960.

NASA SCIENTIFIC AND TECHNICAL PUBLICATIONS

TECHNICAL REPORTS: Scientific and technical information considered important, complete, and a lasting contribution to existing knowledge.

TECHNICAL NOTES: Information less broad in scope but nevertheless of importance as a contribution to existing knowledge.

TECHNICAL MEMORANDUMS: Information receiving limited distribution because of preliminary data, security classification, or other reasons.

CONTRACTOR REPORTS: Technical information generated in connection with a NASA contract or grant and released under NASA auspices.

TECHNICAL TRANSLATIONS: Information published in a foreign language considered to merit NASA distribution in English.

TECHNICAL REPRINTS: Information derived from NASA activities and initially published in the form of journal articles.

SPECIAL PUBLICATIONS: Information derived from or of value to NASA activities but not necessarily reporting the results of individual NASA-programmed scientific efforts. Publications include conference proceedings, monographs, data compilations, handbooks, sourcebooks, and special bibliographies.

Details on the availability of these publications may be obtained from:

SCIENTIFIC AND TECHNICAL INFORMATION DIVISION

NATIONAL AERONAUTICS AND SPACE ADMINISTRATION

Washington, D.C. 20546